International Journal of Hydrogen Energy 126 (2025) 552–561

Contents lists available at ScienceDirect

International Journal of Hydrogen Energy

journal homepage: www.elsevier.com/locate/he

# Enhanced thermal and electrochemical properties in $La_{0.8}Sr_{0.2}MnO_{3-\delta}$-$Pr_6O_{11}$ nanocomposite cathodes for solid oxide fuel cells

Javier Zamudio-García [a,b,*], Leire Caizán-Juanarena [c], Lucía dos Santos-Gómez [b], José M. Porras-Vázquez [b], Enrique R. Losilla [b], David Marrero-López [c]

[a] Department of Energy Conversion and Storage, Technical University of Denmark, Fysikvej, 310, 2800 Kgs., Lyngby, Denmark
[b] Universidad de Málaga, Departamento de Química Inorgánica, Málaga, 29071, Spain
[c] Universidad de Málaga, Departamento de Física Aplicada I, Málaga, 29071, Spain

ARTICLE INFO

Handling Editor: Fanglin F. Chen

*Keywords:*
SOFC
$La_{0.8}Sr_{0.2}MnO_{3-\delta}$
$Pr_6O_{11}$
Nanocomposite
Cathode
Electrode design

ABSTRACT

$La_{0.8}Sr_{0.2}MnO_{3-\delta}$ (LSM)-$Pr_6O_{11}$ nanocomposite electrodes are prepared via a one-step spray-pyrolysis deposition directly onto the electrolyte and evaluated as cathodes for solid oxide fuel cells (SOFCs). The nanoscale integration of two immiscible phases effectively inhibits grain growth while improving mechanical compatibility with the electrolyte. The confinement of the fluorite $Pr_6O_{11}$ phase at the nanoscale during the self-assembly process, achieved by adding the perovskite-type LSM phase with a different crystal structure, hinder the thermally induced phase transitions of $Pr_6O_{11}$ compared to the bulk material. The extended triple-phase-boundary (TPB) in these nanoengineered electrodes leads to exceptional electrochemical performance, achieving a polarization resistance of 0.21 Ω $cm^2$ at 650 °C, significantly lower than the 5.8 Ω $cm^2$ measured for a traditional screen-printed LSM cathode. An anode-supported cell incorporating these nanocomposite electrodes achieves a peak power density of 1.22 W $cm^{-2}$ at 800 °C in wet $H_2$, far exceeding the 0.58 W $cm^{-2}$ observed for the single cell with a commercial LSM electrode under identical conditions. These findings underscore the significant benefits of advanced nanostructured electrode designs and innovative fabrication techniques in achieving high performance and durability in SOFCs.

## 1. Introduction

The growing demand for clean and renewable energy sources has intensified efforts to develop more efficient energy conversion and storage devices [1]. Among these, Solid Oxide Fuel Cells (SOFCs) have garnered significant scientific and technological attention due to their fuel flexibility, high conversion efficiency, and capability to operate in electrolyzer mode [2,3]. However, the major challenge for SOFCs is reducing their operating temperature to the intermediate range (800-600 °C) while maintaining high electrochemical performance [4,5]. Lowering the operating temperature often compromises cell performance, particularly in the air electrode, where the oxygen reduction reaction (ORR) is hindered by slow kinetics [6,7].

In this context, substantial efforts have focused on developing mixed ionic-electronic conductors (MIECs) with improved electrochemical activity at reduced temperatures, such as $La_{0.6}Sr_{0.4}CoO_{3-\delta}$ (LSC), $La_{0.6}Sr_{0.4}Co_{0.2}Fe_{0.8}O_{3-\delta}$ (LSCF), $Sm_{0.5}Sr_{0.5}CoO_{3-\delta}$ (SSC) or $Ba_{0.5}Sr_{0.5}Co_{0.8}Fe_{0.2}O_{3-\delta}$ (BSCF) [8–10]. However, these cobalt-containing materials often exhibit a high thermal expansion mismatch with traditional electrolytes, such as $Zr_{0.84}Y_{0.16}O_{1.92}$ (YSZ) or $Ce_{0.9}Gd_{0.1}O_{1.95}$ (CGO) [6,11]. Additionally, their chemical stability during long-term operation is limited, frequently leading to the formation of Sr-based secondary phases that degrade cell performance. In contrast, traditional $La_{0.8}Sr_{0.2}MnO_{3-\delta}$ (LSM) offers superior stability at high operating temperatures and excellent compatibility with commonly used electrolytes [12]. For this reason, LSM remains the state-of-the-art air electrode material for SOFCs; however, its low ionic conductivity at intermediate temperatures limits its effectiveness compared to the high temperature range [13].

Surface modification via infiltration has emerged as an effective strategy to enhance the electrochemical properties of SOFC cathodes [14]. This process involves preparing aqueous solutions of nitrate salts of the desired elements, followed by infiltration and high temperature calcination to decompose the precursors and achieve phase crystallinity. Recently, the infiltration of praseodymium oxide ($Pr_6O_{11}$) has demonstrated significant improvements in the electrocatalytic activity for the

* Corresponding author. Department of Energy Conversion and Storage, Technical University of Denmark, Fysikvej, Building 310, 2800 Kgs., Lyngby, Denmark.
*E-mail addresses:* javzam@dtu.dk, javi-zamudio@hotmail.com (J. Zamudio-García).

https://doi.org/10.1016/j.ijhydene.2025.04.130
Received 14 February 2025; Received in revised form 5 April 2025; Accepted 7 April 2025
Available online 12 April 2025

oxygen reduction reaction in MIECs or oxide ion-conductors for SOFC, such as $La_{0.6}Sr_{0.4}Co_{0.2}Fe_{0.8}O_{3-\delta}$ [15], $Pr_2(Cu,Ni)O_4$ [16,17], $LaNi_{0.6}Fe_{0.4}O_{3-\delta}$ [18], $PrBaMn_2O_{5+\delta}$ [19] or $Ce_{0.9}Gd_{0.1}O_{1.95}$ [20,21]. This enhancement is attributed to the superior oxygen diffusion and surface exchange coefficients of $Pr_6O_{11}$ at intermediate temperature [22,23]. For instance, Gu et al. [19] observed a significant reduction in polarization resistance for $PrBaMn_2O_{5+\delta}$ after $Pr_6O_{11}$ infiltration, from 1.45 to 0.052 Ω $cm^2$ at 700 °C. Similarly, Ding et al. [18] reported polarization resistance values more than one order of magnitude lower after surface modification of $LaNi_{0.6}Fe_{0.4}O_3$ (LNF) with $Pr_6O_{11}$, decreasing from 1.89 to 0.23 Ω $cm^2$ at 700 °C. However, the infiltrated particles usually exhibit poor adhesion to the host oxide, leading to significant stability issues after long-term operation.

$Pr_6O_{11}$ has also been investigated as an active layer, demonstrating notable performance improvements. For instance, Taguchi et al. [24] explored the effect of different porous active layers (LFN-CGO, $Pr_xCe_{1-x}O_{2-\delta}$ and $Pr_6O_{11}$) on the electrochemical properties of $LaNi_{0.6}Fe_{0.4}O_{3-\delta}$ cathodes. Among these, the electrodes with screen-printed $Pr_6O_{11}$ interlayers achieved the lowest polarization resistance, 0.2 Ω $cm^2$ at 700 °C. However, the high sintering temperature (1000 °C) required to ensure sufficient adhesion to the electrolyte caused reactivity between $Pr_6O_{11}$ and the YSZ electrolyte, resulting in the formation of $Pr_2Zr_2O_7$ and subsequent performance degradation. Alternatively, Sharma et al. [22] prepared porous $Pr_6O_{11}$ active layers at reduced temperatures using electrostatic spray deposition with LSCF as the cathode, achieving remarkable polarization resistance values of 0.02 Ω $cm^2$ at 600 °C and a maximum power density of 500 mW $cm^{-2}$ at 700 °C. Similarly, Kamecki et al. [25] prepared dense $Pr_6O_{11}$ interlayers by spray-pyrolysis to improve the performance of LSCF electrodes, obtaining polarization resistance values of 0.25 Ω $cm^2$ at 600 °C compared to 0.5 Ω $cm^2$ for the bare electrode. However, detailed cross-sectional image analyses revealed cracks and delamination in the $Pr_6O_{11}$ active layer, attributed to the significantly high thermal expansion coefficient (TEC) of the praseodymium oxide system ($PrO_x$). Changes in temperature and oxygen partial pressure can induce polymorphic phase transitions among various praseodymium sub-oxides [26,27], leading to substantial lattice volume changes and significant variations in the TEC values. At temperatures above 480 °C, the TEC of $PrO_x$ reaches $26.0{\cdot}10^{-6}$ $K^{-1}$ [28], which can result in electrode delamination and compromised mechanical integrity.

To improve the mechanical properties of electrodes with high TECs, composite electrodes have been investigated by physically mixing the electrode and electrolyte powders, however, this usually results in non-homogenous materials. An alternative approach is the fabrication of self-assembled nanocomposites in a single preparation step [29]. This results in a homogenous mixture of two phases at the nanoscale level, which has demonstrated remarkable electrochemical performance and durability [29–32]. One of the main advantages of nanocomposite electrodes is the suppressed grain growth during long-term operation, facilitated by the intimate contact between two immiscible phases, which also extends the available active sites for electrochemical reactions. Additionally, nanocomposite electrodes exhibit improved mechanical stability, as the nanoscale interaction between the phases helps limit thermal expansion.

In this work, we present for the first time the successful preparation of self-assembled $La_{0.8}Sr_{0.2}MnO_{3-\delta}$-$Pr_6O_{11}$ nanocomposite electrodes using spray-pyrolysis deposition directly onto the electrolyte at reduced temperatures. The intimate nanoscale interaction between two immiscible phases effectively suppresses grain growth, promotes a more homogeneous distribution of both phases, extends the TPB length for electrochemical reactions and improves mechanical compatibility with the electrolyte. Interestingly, the grain size reduction in the $Pr_6O_{11}$ phase during the self-assembly process, assisted by the incorporation of the perovskite-type LSM phase, suppresses its polymorphic phase transitions to other praseodymium sub-oxides. These improvements are beneficial for avoiding severe mass changes and abrupt TEC changes during thermal cycling, minimizing potential electrode delamination. Furthermore, the extension of the TPB in the nanoengineered electrodes provides more active sites for electrochemical reactions, significantly enhancing performance. The phase formation, crystal structure, thermal properties and microstructure of the self-assembled electrodes were thoroughly investigated and compared with those of conventional electrodes fabricated from powder mixture and screen-printing. The electrochemical properties were extensively examined using impedance spectroscopy and distribution of relaxation times, with particular attention given to the influence of the preparation conditions and electrode microstructure on the electrode response. The performance of the nanocomposite electrodes was evaluated as cathode in anode-supported cells SOFCs.

## 2. Experimental

### 2.1. Materials preparation

Nanocomposite electrodes of LSM−$Pr_6O_{11}$, with LSM:$Pr_6O_{11}$ ratios of 1:0, 1:1, 1:3 and 0:1, were deposited by spray-pyrolysis directly onto dense electrolyte pellets of $Zr_{0.84}Y_{0.16}O_{1.92}$ (YSZ, Tosoh), which were compacted into disks with diameters of 10 mm and thickness of 1 mm and sintered at 1400 °C for 4 h. A 0.025 mol $L^{-1}$ single precursor solution, containing all the cations in stoichiometric amounts, was prepared by dissolving the corresponding metal nitrates: $La(NO_3)_3{\cdot}6H_2O$, $Sr(NO_3)_2$, $Mn(NO_3)_2{\cdot}6H_2O$ and $Pr(NO_3)_3{\cdot}6H_2O$ in Milli-Q water. Nitrate precursors were chosen due to their high solubility in water. In this study, no-toxic solvents were used, making the approach more suitable for potential industrial applications, in contrast to organic solvents such as ethanol or ethylene-glycol, which are commonly employed in literature [22]. Ethylenediaminetetraacetic acid (EDTA) was used as a complexing agent in a 1:4 ligand to metal molar ratio to stabilize the cation solution and promote the formation of crystalline phases after annealing. Precursor solutions with higher EDTA concentrations showed poorer electrode adhesion to the electrolyte due to the significantly higher organic content, leading to excessive electrode porosity during the precursor decomposition. All reagents were supplied by Merck with a minimum purity of 99 %. The resulting precursor solutions were atomized under 2 bars of air pressure using a spray nozzle (nozzle--substrate distance of 20 cm) at a flow rate of 20 mL $min^{-1}$. The samples were deposited for 1 h on quartz and YSZ substrates heated at 250 °C for structural and electrochemical characterization, respectively. Higher deposition temperatures promote further solvent evaporation and precursor decomposition during the spraying process, leading to the formation of dense layers that are unsuitable for electrode applications. Additional details regarding the experimental setup can be found elsewhere [33]. After deposition, samples were calcined in a furnace at 700 °C for 1 h in air, with a heating/cooling rate of 2 °C $min^{-1}$ to achieve crystallization. Different batches of these nanocomposite electrodes, prepared using spray-pyrolysis, demonstrate a good reproducibility confirmed by microstructural and electrochemical characterization.

For thermogravimetric and dilatometric characterization, the same precursor solution used in the spray-pyrolysis process was rapidly frozen into liquid nitrogen by dropwise addition and subsequently dehydrated via vacuum sublimation in a CoolSafe freeze-dryer. The resulting material was calcined at 800 °C for 1 h to produce polycrystalline powders.

For comparison purposes, commercial LSM and $Pr_6O_{11}$ powders were mixed with a binder (Decoflux™) in a ball mill to form an ink, which was then screen-printed onto YSZ pellets and sintered at 1000 °C to ensure proper adhesion to the electrolyte.

### 2.2. Structural and microstructural characterization

Phase formation and crystal structure were analyzed using X-ray powder diffraction (XRD) with an Empyrean PANalytical diffractometer and $CuK_{\alpha1,2}$ radiation. Phase identification was performed using X'Pert

HighScore Plus, while structural analysis was conducted using GSAS software [34].

Electrode morphology was examined using scanning electron microscopy (FE-SEM, Helios Nanolab 650), equipped with an energy-dispersive X-ray spectrometer (EDS, X-Max Oxford) for elemental analysis. Additionally, High-Angle Annular Dark-Field Scanning Transmission Electron Microscopy (HAADF-STEM) was performed using a FEI Talos F200X instrument. For dilatometry measurements, ceramic bars of 15 mm in length were prepared and sintered at 1000 °C. The dilatometric curves were recorded in air atmosphere using a Netzsch DIL 402 instrument at a heating rate of 3 °C $min^{-1}$ over a temperature range of 20–800 °C. Thermogravimetric analysis (TG) and differential scanning calorimetry (DSC) were simultaneously recorded using a STA 449 F3 Jupiter instrument under air atmosphere, with a heating rate of 3 °C $min^{-1}$ over the same temperature range.

### 2.3. Electrochemical characterization

Electrode polarization resistance was determined using Electrochemical Impedance Spectroscopy (EIS) in a symmetrical cell configuration. Measurements were conducted with a frequency response analyzer (Solartron 1260 FRA) over a frequency range of 0.01 Hz–$10^6$ Hz, with an AC perturbation of 50 mV. Data were collected under open circuit voltage in air, covering a temperature range from 750 to 450 °C on cooling, with a 30 min dwell time between successive measurements. Platinum ink and meshes were used to ensure homogenous current collection. Impedance spectra were also recorded as a function of the oxygen partial pressure ($pO_2$) to identify the electrochemical processes involved in oxygen reduction reactions (ORR). The Distribution of relaxation times (DRT) method was employed to distinguish the different electrochemical processes contributing to the electrode response [35]. The EIS data were fitted using equivalent circuit models with the ZView software [36].

The performance of the nanocomposite electrodes under SOFC operating conditions was evaluated using anode-supported SOFCs with a Ni-YSZ/YSZ/LSM-$Pr_6O_{11}$ configuration. Commercial Ni-YSZ/YSZ anode-supported cells, supplied by Ningbo SOFCMAN, were employed for single-cell tests (square cells, 15×15 $mm^2$). The LSM−$Pr_6O_{11}$ nanocomposite cathodes developed in this work were deposited onto the commercial half-cells using the spray-pyrolysis method described earlier. The full cells were sealed to a tubular alumina test chamber using a ceramic paste (Ceramabond 668, Aremco). Current-voltage and impedance data were collected with a Zahner Zennium XC over the temperature range of 800-650 °C, using $H_2$ (3 vol% water) as the fuel and air as oxidant. For comparison, a single cell with a screen-printed commercial LSM cathode (Praxair) was also prepared and tested under identical conditions. The cathode active area was limited to 0.25 $cm^2$ for both cells.

## 3. Results and discussion

### 3.1. Structural and microstructural characterization

XRD patterns of the nanocomposite electrodes with different LSM: $Pr_6O_{11}$ ratios, deposited onto quartz wafers and YSZ electrolytes using spray-pyrolysis, are shown in Fig. 1a and Fig. S1, respectively. The $Pr_6O_{11}$ single-phase electrode crystallizes in a cubic fluorite structure (s.g. $Fm\bar{3}m$), while the LSM layer adopts a rhombohedral perovskite-type structure (s.g. $R\bar{3}c$). The self-assembled nanocomposites consist of a mixture of these two crystalline phases, which are clearly identified as fluorite and perovskite phases, with no evidence of secondary phases or additional reflections (Fig. 1a).

The XRD patterns of the LSM-$Pr_6O_{11}$ nanocomposites were analyzed using the Rietveld method (Fig. 1b, Fig. S2). The unit cell volume of the LSM film at 700 °C was 350.22(2) $Å^3$, which is consistent with literature values [37,38]. However, the LSM phase in the nanocomposite electrode showed a slight decrease in cell volume with the addition of $Pr_6O_{11}$, from 347.64(2) $Å^3$ for LSM-$Pr_6O_{11}$ (1:1) to 345.95 (2) $Å^3$ for LSM-$Pr_6O_{11}$

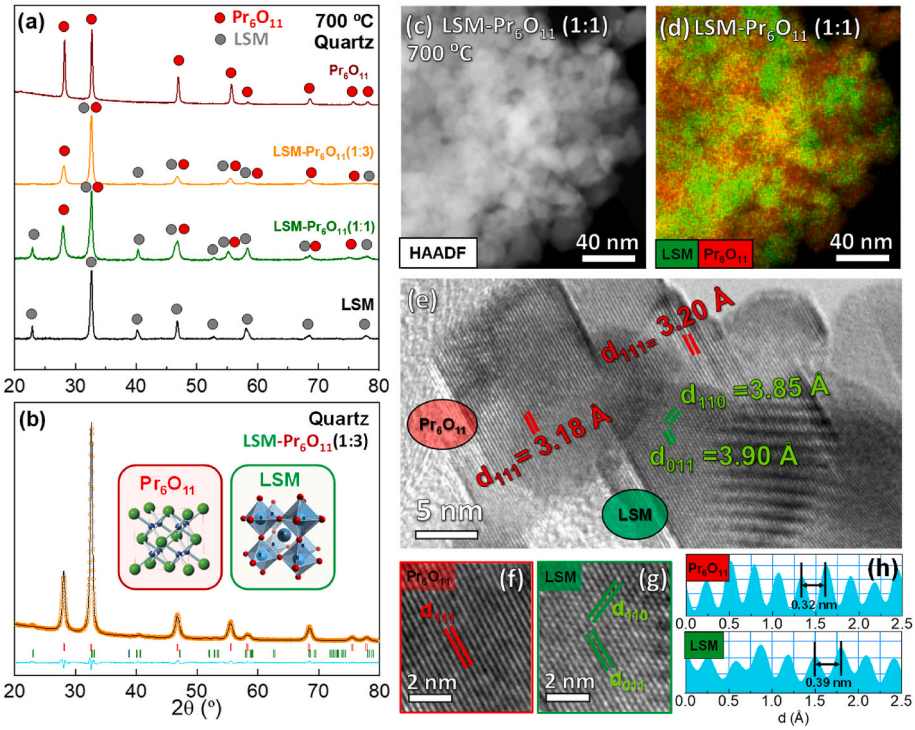


**Fig. 1.** (a) XRD patterns of LSM-$Pr_6O_{11}$ electrodes deposited onto quartz wafer using spray-pyrolysis. (b) Representative Rietveld refinement of the LSM-$Pr_6O_{11}$ (1:3) nanocomposite. (c) HAADF-STEM image of the LSM-$Pr_6O_{11}$ (1:1) nanocomposite calcined at 700 °C and (d) the corresponding EDS mapping revealing homogenous phase distribution. (e) HRTEM image of the nanocomposite electrode, highlighting the atomic ordering for (f) $Pr_6O_{11}$, (g) LSM, and (h) the corresponding line scan showing the interatomic distances.

(1:3). This variation suggests minor cation incorporation of praseodymium into LSM during the synthesis process. Since the ionic radii of $Pr^{3+}$ (1.32 Å) is smaller than that of $La^{3+}$ (1.36 Å) in twelve-fold coordination, this incorporation accounts for the observed decrease in LSM cell volume. Such minor cation interdiffusion is not expected to negatively impact the electrochemical properties. In fact, it may enhance the ORR kinetics due to the high electrocatalytic activity of mixed $Pr^{3+}/Pr^{4+}$ ions, as previously demonstrated in various perovskite-type cathode materials [39–41].

The phase fraction, calculated by the Rietveld method, closely matches the nominal value (Table S1), confirming the composition of the nanocomposite electrodes. The $R_{wp}$ disagreement factor ranged from 1.8 to 7.3 %, indicating good fitting accuracy regardless of electrode composition. The crystallite size, calculated using the Scherrer's equation, is significantly smaller for the nanocomposite electrodes compared to single-phase materials, with values as low as 16.1 and 14.8 nm for the LSM and $Pr_6O_{11}$ components, respectively. This behavior is attributed to the nanoscale contact between the two immiscible phases, which limits grain growth by restricting cation diffusion [29,42]. Similar findings were observed for the LSM-$Pr_6O_{11}$ nanocomposite electrodes deposited onto YSZ electrolytes. In the Rietveld analysis, an additional YSZ phase (s.g. $Fm\bar{3}m$) was included to account for the substrate. The unit cell volumes for the samples were similar to those on quartz, as shown in Table S1, with representative Rietveld plots presented in Fig. S3.

Phase formation in the self-assembled nanocomposite electrodes was further investigated using transmission electron microscopy. HAADF-STEM and EDS analysis revealed well-defined phase boundaries with strong interphase contact induced by the self-assembly preparation process and confirmed the homogenous distribution of LSM and $Pr_6O_{11}$ nanoparticles (Fig. 1c and d). The coexistence of two phases at the nanoscale not only limits the grain growth but also leads to a significant extension of the TPB compared to conventional composite materials, which are typically obtained by physically mixing micrometric powders. HRTEM imaging reveals that the nanocomposite consists of plate-shaped particles of approximately 10 nm in diameter (Fig. 1e), consistent with XRD observations, with no visible formation of amorphous domains. The crystal structure and interatomic distances correspond to those expected for cubic fluorite and rhombohedral perovskite-type structures (Fig. 1f–h).

Cross-sectional SEM images reveal significant microstructural differences between the electrodes prepared by traditional screen-printing and spray-pyrolysis (Fig. 2). The composite electrodes prepared by screen-printing were obtained by physically mixing electrode and electrolyte powders, requiring high annealing temperatures (1000 °C) to ensure adequate adhesion to the electrolyte. These high calcination temperatures promote grain growth and reduce electrode porosity, which decreases the triple phase boundary (TPB) for electrochemical reactions, ultimately lowering the overall electrode performance. The $Pr_6O_{11}$ electrode, has a thickness of approximately 15 μm, high porosity and good adhesion to the electrolyte (Fig. 2a and b). Higher magnification images show that the screen-printed electrode is composed of micrometer-sized particles larger than 1 μm in diameter. Similar findings are observed for the LSM electrode, also deposited by screen-printing, with particles around 300 nm (Fig. 2c and d).

In contrast, nanocomposites electrodes prepared by spray-pyrolysis from aqueous precursor solutions were directly deposited onto the electrolyte, requiring significantly lower calcination temperatures (700 °C). The $Pr_6O_{11}$ electrode prepared in a single-step by spray-pyrolysis shows a vertical laminar morphology with strong adhesion to the electrolyte (Fig. S4). The nanocomposite electrode features a significantly smaller particle size of approximately 40 nm and a thickness of 15 μm, while maintaining good adhesion and sufficient porosity (Fig. 2e and f). The deposition of self-assembled nanocomposite electrodes at a reduced temperature directly on the electrolyte not only prevents excessive grain growth but also increases the density of active sites for electrochemical reactions. These results clearly evidence the significant influence of the preparation method on electrode morphology, which in turn greatly affects electrode performance.

Thermogravimetric-differential scanning calorimetry curves (TG-DSC) provide further insights into the structure and phase transformations in the LSM-$Pr_6O_{11}$ electrodes (Fig. 3a and b). The physically mixed $Pr_6O_{11}$-containing samples show exothermic peaks upon cooling at ~ 430 and 695 °C, accompanied by mass changes due to oxygen release as $Pr^{4+}$ is thermally reduced to $Pr^{3+}$ [26,27]. These transformations are reversible upon heating and cooling (Fig. S5). As previously indicated, praseodymium oxides ($PrO_x$) consist of sub-oxides with a fluorite structure, adjusting their oxygen content with the annealing temperature. The $Pr_6O_{11}$ phase is stable in air below 400 °C, while

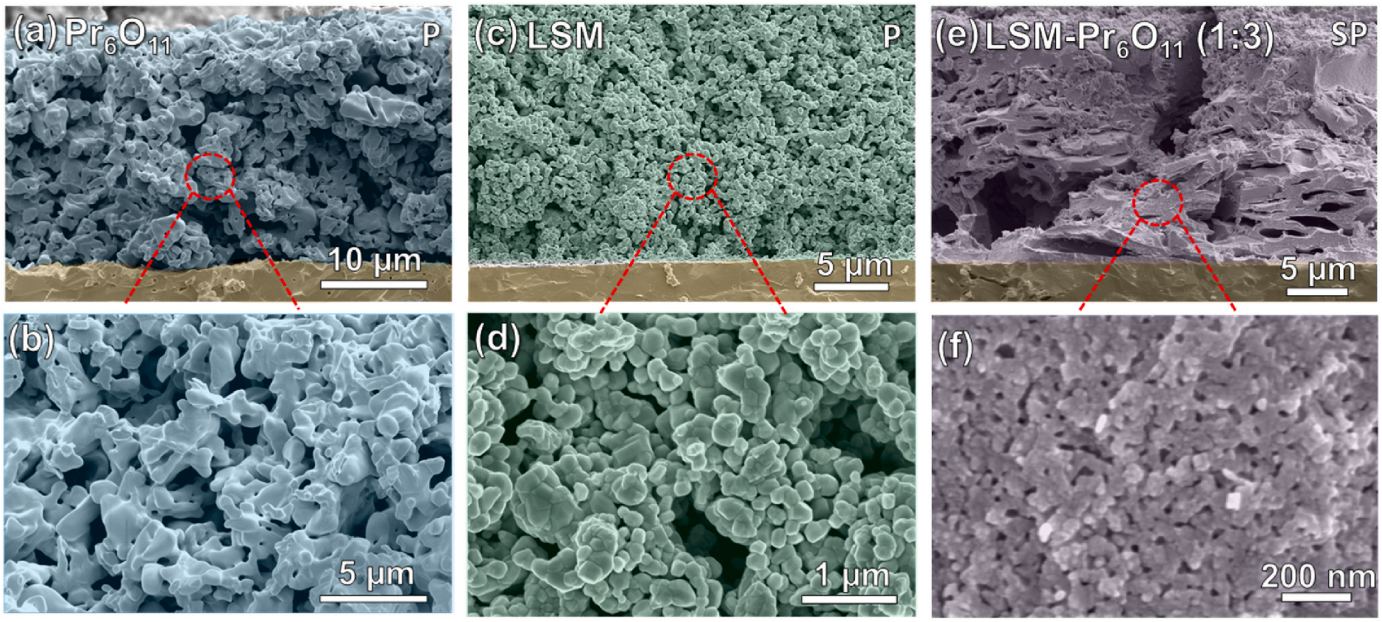


**Fig. 2.** Cross-sectional SEM images at different magnifications of (a,b) $Pr_6O_{11}$ and (c,d) LSM deposited by screen-printing and calcined at 1000 °C. (e,f) LSM-$Pr_6O_{11}$ (1:3) nanocomposite electrode deposited by spray-pyrolysis at 250 °C and calcined at a reduced temperature of 700 °C.

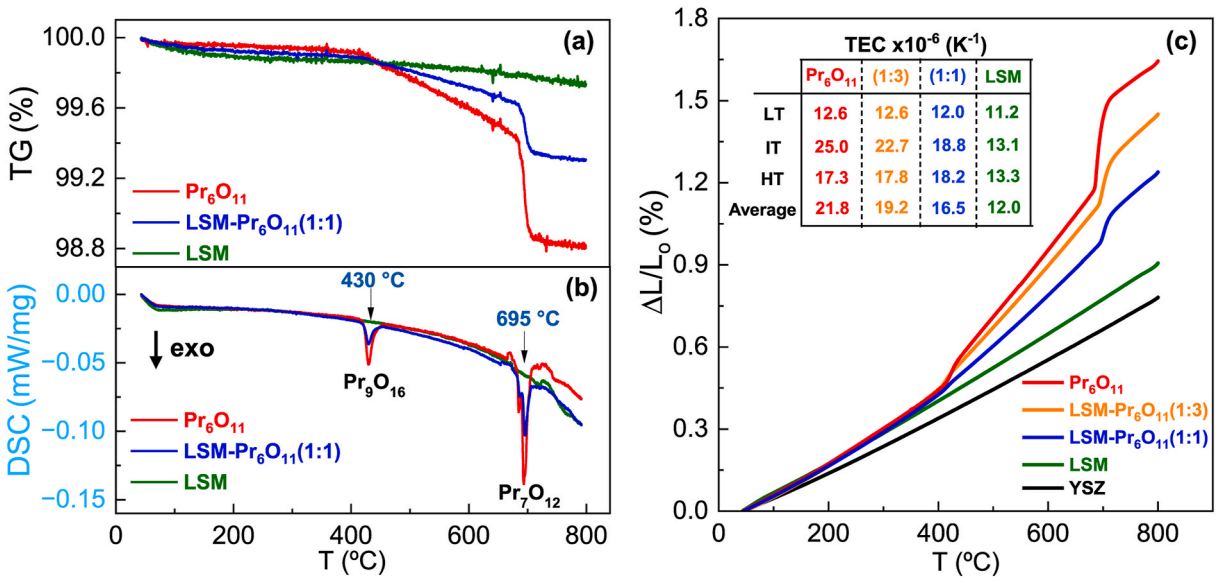


**Fig. 3.** (a) TG and (b) DSC curves in air for the LSM-$Pr_6O_{11}$ composite electrodes obtained from mixed powders, recorded in the temperature range of 30–800 °C during cooling. (c) Dilatometric curves for LSM-$Pr_6O_{11}$ electrodes prepared from mixed powders. The inset shows a table with the thermal expansion coefficients (TEC) for different temperature ranges: LT (<400 °C), IT (400–700 °C) and HT (>700 °C).

$Pr_9O_{16}$ predominates between 430 and 700 °C [43]. The average oxidation states for $Pr_6O_{11}$ and $Pr_9O_{16}$ are close to 3.667 and 3.556, respectively [43]. Above 700 °C, the oxygen content readjusts, forming $Pr_7O_{12}$ with a significant mass change [43,44].

The thermal expansion behavior of LSM-$Pr_6O_{11}$ electrodes further confirms these phase transformations (Fig. 3c). Three regions with different slopes are observed. At low temperatures, all samples exhibited similar TEC values, ranging from 11.6 to $12.6{\cdot}10^{-6}$ $K^{-1}$. However, at higher temperatures, the TEC increases significantly, in line with the higher mass loss observed in the TG curves, reaching $25{\cdot}10^{-6}$ $K^{-1}$ for $Pr_6O_{11}$ at intermediate temperatures. The average TEC values of $\sim 21.8{\cdot}10^{-6}$ $K^{-1}$ for $Pr_6O_{11}$ is consistent with that reported by Chen et al. [28], and comparable to Co-based cathodes, such as $La_{0.6}Sr_{0.4}CoO_{3-\delta}$ ($23.0{\cdot}10^{-6}$ $K^{-1}$ [45]), $Sm_{0.5}Sr_{0.5}CoO_{3-\delta}$ ($25.5{\cdot}10^{-6}$ $K^{-1}$ [46]) or $PrBaCo_2O_{5+\delta}$ ($24.0{\cdot}10^{-6}$ $K^{-1}$ [47]). As expected, the incorporation of LSM progressively reduces the average TEC values from 19.2 to $16.5{\cdot}10^{-6}$ $K^{-1}$, for LSM-$Pr_6O_{11}$ (1:3) and (1:1), respectively. This reduction in TEC values enhances mechanical stability during thermal cycling, addressing a major constraint of $Pr_6O_{11}$-based functional layers despite their fast ORR kinetics [22].

Interestingly, the self-assembled nanocomposite electrodes, composed of nanosized particles, show no thermal transformation in the DSC and no abrupt slope changes in the dilatometry curves (Fig. S6). This suggests stabilization of the high temperature $PrO_x$ phase at room

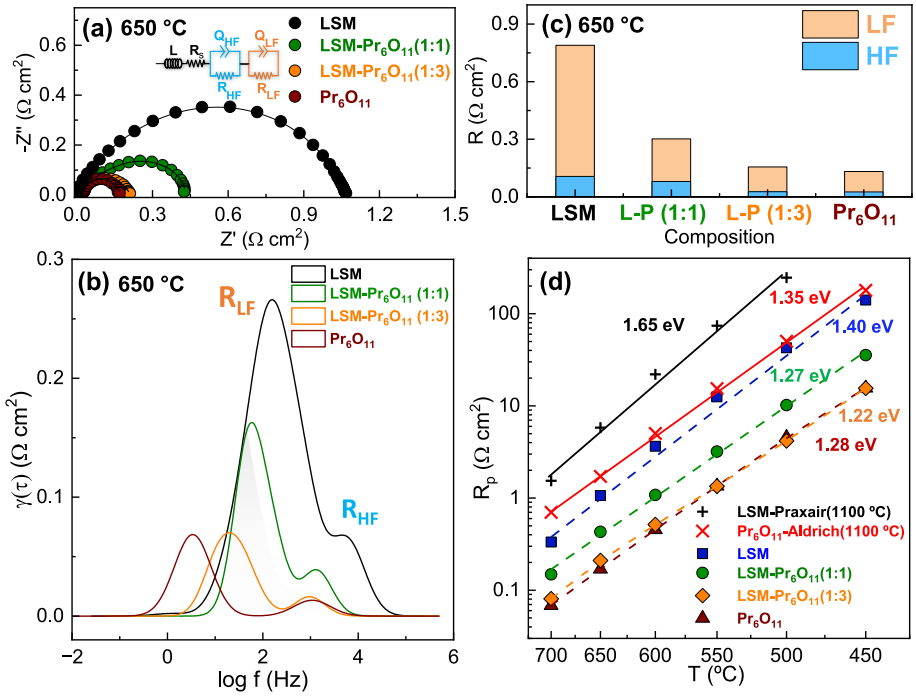


**Fig. 4.** (a) Impedance spectra at 650 °C in air of LSM-$Pr_6O_{11}$ (L–P) nanocomposite electrodes prepared by spray-pyrolysis, with the corresponding (b) DRT analysis. (c) Bar graphic showing the HF and LF electrode resistance contributions. (d) Arrhenius plots of the overall electrode polarization resistance in air.

temperature in nanocrystalline samples, similar to the stabilization of the cubic phase in LSCF nanostructured electrodes [48]. The nanoscale confinement of the fluorite $Pr_6O_{11}$ phase, achieved by incorporating LSM phase with a different crystal structure, hinders thermal-driven atomic level reorganization, making phase transition more difficult compared to bulk materials. This suppression of phase transitions is beneficial for improving mechanical properties and preventing electrode delamination during thermal cycling.

### 3.2. Electrochemical characterization

Fig. 4a shows the impedance spectra of the different electrodes deposited by spray-pyrolysis, measured at 650 °C in air. The LSM-$Pr_6O_{11}$ nanocomposite electrodes exhibit significantly lower electrode polarization resistance compared to blank LSM. Fig. 4b presents the DRT spectra at 650 °C for LSM:$Pr_6O_{11}$ nanocomposite electrodes, all fabricated by spray-pyrolysis. Interestingly, both electrode contributions decrease as the $Pr_6O_{11}$ content increases. The addition of the $Pr_6O_{11}$ phase, known for its high ionic-conductivity, extends the TPB beyond the electrode/electrolyte interphase by providing a higher concentration of active sites for ORR and creating more efficient oxide-ion transport pathways to the electrode surface. This enhanced electrocatalytic activity on the electrode surface correlates with the smaller contribution of low-frequency (LF) process, centered around 100 Hz [38,49]. Additionally, improved oxide ion transport at the electrode/electrolyte interface leads to reduced contribution of the high frequency (HF) process, centered at $10^4$ Hz [50,51]. Overall, the incorporation of $Pr_6O_{11}$ in the nanocomposite electrode significantly influences both high- and low-frequency electrode responses. $Pr_6O_{11}$, with high oxide-ion conductivity, provides faster ionic transport pathways at the interface, overcoming the ionic transport limitations of LSM, which predominantly exhibits electronic conductivity at intermediate temperatures. Additionally, the homogeneous nanoscale interaction between $Pr_6O_{11}$ and LSM minimizes grain growth and increases the available active sites for electrochemical reactions, thereby enhancing the surface kinetics for ORR, which is identified as the low-frequency process.

Fig. 4c presents a bar graph illustrating the resistance contributions for each electrode composition at 650 °C. The LF process is the dominant contribution to the total polarization resistance, shifting progressively to higher frequencies as the temperature decreases (Fig. S7) [52], indicating slower electrode kinetics [4]. Based on DRT data, the electrode response is effectively modeled using an equivalent circuit with two RQ elements in series (inset Fig. 4a), where each R represents a resistance in parallel with a constant phase element, Q.

Fig. 4d compares the temperature dependence of the overall polarization resistance ($R_p$) in air. Commercial LSM deposited by screen-printing exhibits poor electrochemical performance at intermediate temperatures, with an $R_p$ of 5.80 Ω cm$^2$ at 650 °C. Spray-pyrolysis deposition significantly improves LSM performance, reducing $R_p$ to 1.06 Ω cm$^2$ at 650 °C. Nanocomposite electrodes prepared by spray-pyrolysis show even greater enhancements, achieving an $R_p$ of 0.21 Ω cm$^2$ at 650 °C for LSM-$Pr_6O_{11}$ (1:3). Although $Pr_6O_{11}$ electrode prepared by spray-pyrolysis shows slightly lower $R_p$ values (0.17 Ω cm$^2$ at 650 °C), the use of pure $Pr_6O_{11}$ in SOFCs is limited by its low electronic conductivity (0.5 S cm$^{-1}$ at 700 °C [21]) and its relatively high thermal expansion coefficient (see Fig. 3c). Additionally, $Pr_6O_{11}$ undergoes polymorphic phase transitions on heating, as previously discussed, leading to significant lattice volume changes that compromise the mechanical stability.

The LSM-$Pr_6O_{11}$ (1:3) nanocomposite electrode exhibits a lower activation energy (1.22 eV), which is considerably lower than that of traditional LSM (1.65 eV), $Pr_6O_{11}$ (1.35 eV), or other composite materials reported in literature, such as LSM-YSZ (1.53 eV), LSM-SDC (1.32 eV) or LSM-$Bi_{1.76}Dy_{0.16}Y_{0.08}O_{3-\delta}$ (1.38 eV) [37]. The polarization resistance values achieved in this work are lower than those reported for LSM-based composite electrodes in recent literature, such as LSM-SDC (3 Ω cm$^2$ at 650 °C [53]) LSM-$Bi_{1.76}Dy_{0.16}Y_{0.08}O_{3-\delta}$ (0.519 Ω cm$^2$ at 650 °C [37]), LSM-YSZ decorated with $PrO_x$ nanoparticles (0.6 Ω cm$^2$ at 650 °C [54]) and LSM-YSZ nanofibers (0.65 Ω cm$^2$ at 650 °C [55]).

To gain a deeper understanding of the electrode processes involved in ORR, the impedance spectra at 650 °C were measured at varying oxygen partial pressures ($pO_2$) (Fig. 5a). The relationship between the resistance of each electrode contribution and $pO_2$ is expressed as $R_{HF,LF} \sim (pO_2)^{-m}$, where the exponent $m$ provides insights into the species participating in each ORR sub-reaction (Table S2).

DRT analysis of the impedance spectra as a function of the $pO_2$ reveals two electrode contributions (Fig. 5b), as discussed previously. The high frequency (HF) response is almost independent of $pO_2$ ($m \sim 0$), indicating that atomic or molecular oxygen is not involved in this sub-reaction (Fig. 5c). This suggests that the HF process corresponds to the transport of oxide ions from the TPB to the electrolyte ($O^{2-}_{TPB} \rightarrow O^{x}_{o,\,electrolyte}$) [56,57]. In contrast, the low frequency (LF) process dominates the total polarization resistance and exhibits a strong dependence on $pO_2$, with a reaction order of $m \sim 0.5$. This indicates that the LF process is related to oxygen dissociation at the electrode surface ($O_{2,\,ad} \rightarrow 2O_{ad}$) [58,59]. Interestingly, as $pO_2$ increases, the LF process shifts to higher frequencies, reflecting a lower relaxation time and faster electrode kinetics. Fig. 5d illustrates the electrochemical results, and Table S2 summarizes the different rate-determining steps for the ORR.

The efficiency of the nanocomposite electrodes was evaluated in fuel cell mode using an anode-supported cell: Ni-YSZ/YSZ/LSM-$Pr_6O_{11}$ (1:3). For comparison, a cell with the screen-printed LSM cathode was tested under identical conditions. Fig. 6a and b compares the current-voltage and power density curves for the cells with LSM and LSM-$Pr_6O_{11}$ (1:3) electrodes prepared by screen-printing and spray-pyrolysis, respectively. The open circuit voltage (OCV) at 700 °C was 1.115 V for the LSM-$Pr_6O_{11}$ (1:3) and 1.113 V for LSM cell, respectively, which is consistent with the theoretical Nernst value for wet hydrogen (3 vol% $H_2O$) as fuel and air as the oxidant, confirming proper cell sealing.

The peak power densities achieved by the cell with self-assembled LSM-$Pr_6O_{11}$ (1:3) nanocomposite electrode were 1.22 and 0.74 W cm$^{-2}$ at 800 and 700 °C, respectively, significantly outperforming the cell with screen-printed LSM electrode, which delivered 0.58 and 0.33 W cm$^{-2}$ at 800 and 700 °C, respectively (Fig. S8). Since the anode and the electrolyte are identical, these differences in power density are attributed to the enhanced performance of the nanocomposite cathode. This performance also exceeds that of recently reported LSM-based electrodes, such as LSM-YSZ nanocomposite (0.83 W cm$^{-2}$ at 800 °C [60]), LSM-YSZ nanofibers (1.15 W cm$^{-2}$ at 800 °C [55]), LSM-YSZ decorated with $PrO_x$ nanoparticles (0.42 W cm$^{-2}$ at 650 °C [54]), LSM-$Bi_{1.5}Y_{0.5}O_3$ (0.66 W cm$^{-2}$ at 700 °C [61]) and $Pr_6O_{11}$ (0.50 W cm$^{-2}$ at 700 °C [22]) (Table 1).

Fig. 6c shows the impedance spectra for the cells at 750 °C under OCV. Both cells exhibit comparable ohmic resistance (~0.15 Ω cm$^2$ at 750 °C), consistent with the expected value for a 10 μm thick YSZ electrolyte. However, the total polarization resistance for the cell with LSM-$Pr_6O_{11}$ (1:3) cathode is significantly lower (0.43 Ω cm$^2$) compared to the cell with LSM cathode (1.10 Ω cm$^2$). Fig. 6e shows the DRT spectra at 750 °C of single cells with traditional LSM deposited by screen-printing and LSM:$Pr_6O_{11}$ (1:3) nanocomposite electrode prepared by spray-pyrolysis. The high frequency electrode contribution ($R_{HF}$), attributed to oxide-ion transport at the electrode-electrolyte interphase, is notably higher in the cell with the screen-printed LSM cathode. This slower ionic transport kinetics can be attributed to the inherent low ionic conductivity of LSM, which limits the TPB to the interphase. In contrast, the incorporation of $Pr_6O_{11}$ at the nanoscale level facilitates coherent oxide-ion conduction pathways to the electrolyte, unlike single-phase LSM, which predominantly exhibits electronic conductivity. Additionally, surface kinetics at the cathode surface ($R^{cat}_{LF}$) benefit from the increased TPB length in the nanocomposite. In contrast, the resistance associated with the hydrogen oxidation reaction in the fuel electrode ($R^{an}_{LF}$), centered at 1 Hz, remains similar, confirming that the

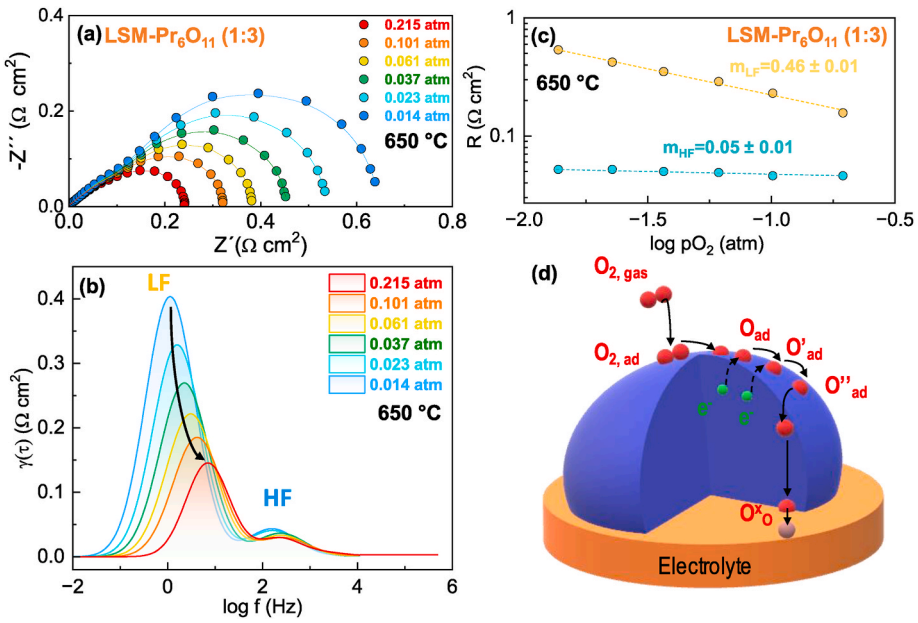


**Fig. 5.** (a) Impedance spectra of LSM-$Pr_6O_{11}$(1:3) nanocomposite at 650 °C in air, with the corresponding (b) DRT spectra and (c) electrode resistance contributions as a function of $pO_2$ at 650 °C (d) Illustration showing the different rate-limiting steps for the ORR.

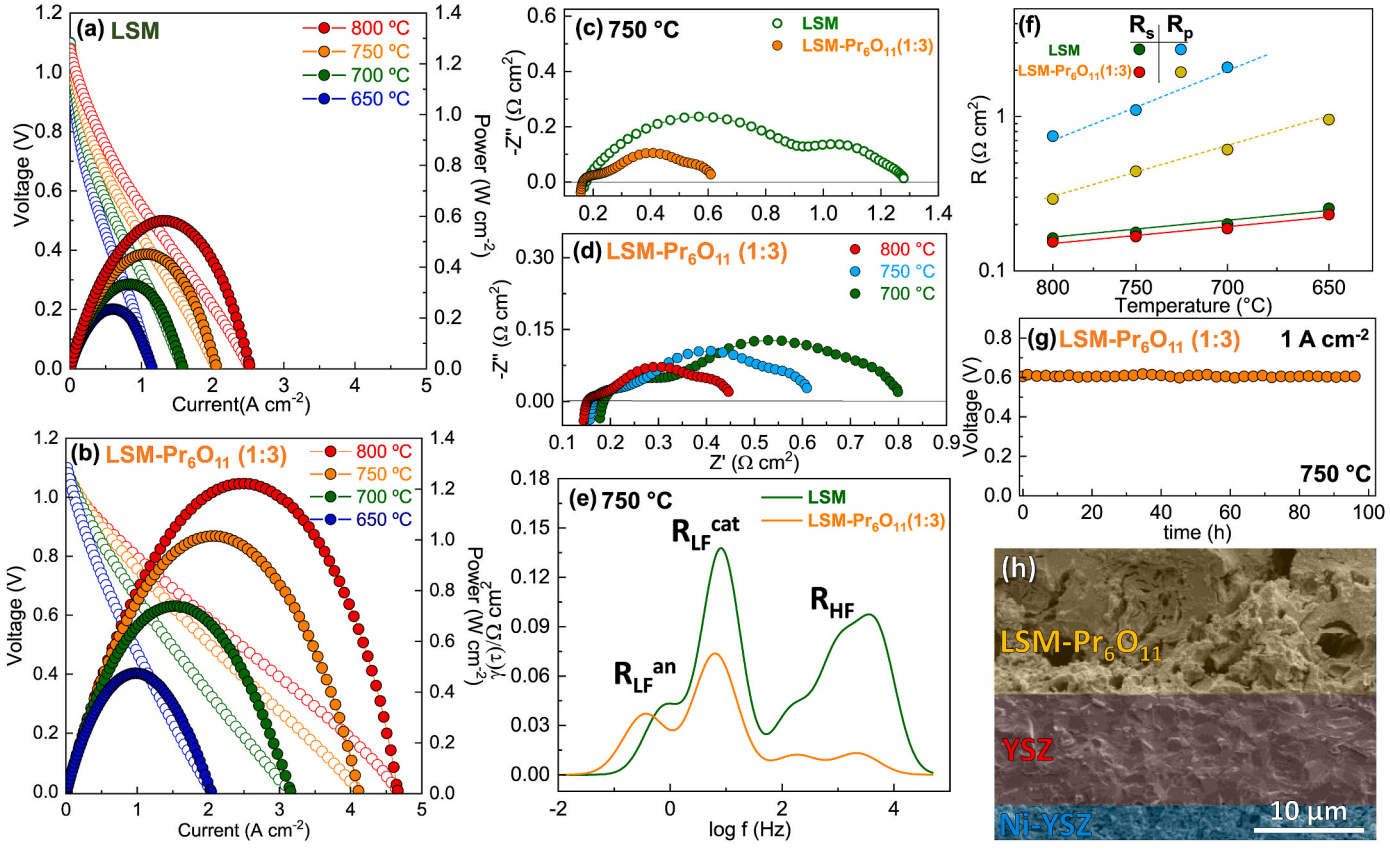


**Fig. 6.** Current-voltage and power density curves of anode-supported cells with (a) screen-printed LSM cathode and (b) LSM-$Pr_6O_{11}$ (1:3) nanocomposite electrode prepared by spray-pyrolysis. (c) Impedance spectra at 750 °C at OCV for both cells. (d) Impedance spectra for the LSM-$Pr_6O_{11}$ (1:3) nanocomposite cell at different temperatures. (e) DRT curves for both cells at 750 °C. (f) Variation of the ohmic ($R_s$) and electrode polarization ($R_p$) resistances with the temperature for both cells. (g) Durability test for 100 h at 750 °C at a current density of 1 A $cm^{-2}$. (h) Cross-sectional SEM images of the LSM-$Pr_6O_{11}$ (1:3) cell after electrochemical testing.

enhanced performance is due to the nanocomposite cathode.

Fig. 6d shows the impedance spectra for the cell with the LSM-$Pr_6O_{11}$ (1:3) electrode at different temperatures. As the temperature decreases, electrode polarization resistance increases due to the slower electrode kinetics, which significantly affects the cell performance at intermediate temperatures (Fig. 6f). However, the ohmic resistance increases slightly

**Table 1**
Electrochemical properties of several LSM-based electrodes for SOFCs. Polarization resistance values ($R_p$) in air are given at 700 °C in symmetrical configuration, and otherwise, temperature is specified. Power density values for Ni-YSZ/YSZ supported cells are included at 700 °C and 800 °C.

| Anode | YSZ Electrolyte thickness (μm) | Electrode | Sintering temperature (°C) | $R_p$ (Ω cm$^2$) | Power density (W cm$^{-2}$) | Ref. |
|---|---|---|---|---|---|---|
| Ni-YSZ | 10 | LSM | 1000 | $1.54^{700\ °C}$ | $0.58^{800\ °C}$<br>$0.33^{700\ °C}$ | This work |
| Ni-YSZ | 10 | LSM-$Pr_6O_{11}$ (1:3) (nanocomposite) | 700 | $0.08^{700\ °C}$ | $1.22^{800\ °C}$<br>$0.74^{700\ °C}$ | This work |
| Ni-YSZ | 20 | LSM | 950 | $4.00^{700\ °C}$ | $0.34^{800\ °C}$ | [62] |
| Ni-YSZ | 10 | $Pr_6O_{11}$ | 700 | $0.03^{600\ °C}$ | $0.50^{700\ °C}$ | [22] |
| Ni-YSZ | 10 | LSM + YSZ (composite) | 1200 | – | $0.47^{800\ °C}$<br>$0.25^{700\ °C}$ | [63] |
| Ni-YSZ | 10 | LSM + YSZ (nanocomposite) | 850 | – | $0.83^{800\ °C}$<br>$0.21^{700\ °C}$ | [60] |
| Ni-YSZ | 3 | LSM + YSZ (nanofibers) | 1200 | $0.18^{700\ °C}$ | $1.15^{800\ °C}$ | [55] |
| Ni-YSZ | 13 | LSM + CGO (composite) | 1150 | – | $0.20^{800\ °C}$ | [64] |
| Ni-YSZ | 13 | LSM + SDC (infiltration) | 1150 | – | $1.32^{800\ °C}$<br>$0.72^{700\ °C}$ | [65] |
| Ni-YSZ | 10 | LSM + YSB (composite) | 1050 | $0.10^{700\ °C}$ | $0.66^{700\ °C}$ | [61] |
| Ni-YSZ | 15 | LSM + ESB (composite) | 850 | $0.22^{700\ °C}$ | $0.74^{700\ °C}$ | [66] |
| Ni-YSZ | – | LSM + YSB (composite) | 800 | $0.4^{700\ °C}$ | $0.78^{700\ °C}$ | [67] |

as the temperature decreases. DRT analysis reveals that reduced electrocatalytic activity at both the cathode ($R_{LF}^{cat}$) and anode ($R_{LF}^{an}$) surface at lower temperatures is the main contribution to the overall polarization resistance. In contrast, the high frequency contributions ($R_{HF}$), related to interfacial processes, are minimally affected by temperature changes (Fig. S9).

The durability of the LSM-$Pr_6O_{11}$ (1:3) cell was evaluated under continuous operation at a constant current density of 1 A cm$^{-2}$ at 750 °C. Over a period of 100 h, the cell voltage remained stable, demonstrating the excellent long-term stability of the nanocomposite cathode (Fig. 6g). Cross-sectional SEM images of the Ni-YSZ/YSZ/LSM-$Pr_6O_{11}$ (1:3) (Fig. 6h) and Ni-YSZ/YSZ/LSM cells (Fig. S10) after the electrochemical tests show a strong adhesion between the cell layers, with no visible cracks or delamination. These results highlight the robustness and reliability of the nanocomposite electrode under extended operating conditions, surpassing the limitations of the corresponding bulk materials, which exhibit higher TEC coefficients and thermal phase transformations.

## 4. Conclusions

LSM−$Pr_6O_{11}$ self-assembled nanocomposite electrode layers were prepared via single-step spray-pyrolysis directly onto the electrolyte and tested as cathodes for SOFCs. The nanoengineered electrodes, with immiscible phases in nanoscale contact, effectively suppressed grain growth and enhanced mechanical compatibility with the electrolyte. The addition of LSM significantly reduced the thermal expansion coefficients, addressing key challenges associated with $Pr_6O_{11}$-based functional layers. Additionally, the nanocrystalline nature of the self-assembled electrodes stabilized the high temperature $Pr_6O_{11}$ polymorph at room temperature, preventing phase transitions below 800 °C and mitigating abrupt changes in TEC values.

The seamless integration of ionic and electronic conducting phases extended the active TPB, promoting efficient surface electrochemical reactions and facilitating rapid oxide-ion transport across the interface. The nanocomposite electrodes exhibited a polarization resistance of 0.21 Ω cm$^2$ at 650 °C, significantly lower than the 5.8 Ω cm$^2$ observed for a screen-printed LSM electrode. An anode-supported Ni-YSZ/YSZ/LSM-$Pr_6O_{11}$ (1:3) cell achieved a remarkable peak power density of 1.22 W cm$^{-2}$ at 800 °C, considerably higher than the 0.58 W cm$^{-2}$ achieved by a single cell with a screen-printed LSM electrode at the same temperature. This approach not only enhances the mechanical compatibility of electrodes with high TECs but also optimizes the TPB through the synergistic combination of ionic and electronic conducting pathways at the nanoscale. These findings underscore the significant advantages of nanostructured electrode designs for enhancing both performance and durability in SOFCs.

## CRediT authorship contribution statement

**Javier Zamudio-García:** Writing – original draft, Methodology, Investigation, Formal analysis, Conceptualization. **Leire Caizán-Juanarena:** Writing – review & editing, Methodology, Investigation. **Lucía dos Santos-Gómez:** Writing – review & editing, Investigation. **José M. Porras-Vázquez:** Writing – review & editing. **Enrique R. Losilla:** Writing – review & editing. **David Marrero-López:** Writing – review & editing, Project administration, Methodology, Funding acquisition, Conceptualization.

## Declaration of competing interest

The authors declare that they have no known competing financial interests or personal relationships that could have appeared to influence the work reported in this paper.

## Acknowledgements

The authors acknowledge the grants PID2021–126009OB-I00 and TED2021-129836B–I00, funded by MCIN/AEI/10.13039/501100011033 and by "ERDF A way of making Europe", by the European Union. J.Z.G thanks to the Spanish Ministry of Education, Culture and Sport for his FPU grant (FPU17/02621) and his postdoctoral contract at Technical University of Denmark (DTU).

## Appendix A. Supplementary data

Supplementary data to this article can be found online at https://doi.org/10.1016/j.ijhydene.2025.04.130.

## References

[1] Xu Y, Cai S, Chi B, Tu Z. Technological limitations and recent developments in a solid oxide electrolyzer cell: a review. Int J Hydrogen Energy 2024;50:548–91. https://doi.org/10.1016/j.ijhydene.2023.08.314.
[2] Shi H, Tang J, Yu W, Tadé MO, Shao Z. Advances in power generation from ammonia via electrocatalytic oxidation in direct ammonia fuel cells. Chem Eng J 2024;488:150896. https://doi.org/10.1016/j.cej.2024.150896.
[3] Zamudio-García J, Caizán-Juanarena L, Porras-Vázquez JM, Losilla ER, Marrero-López D. A review on recent advances and trends in symmetrical electrodes for solid oxide cells. J Power Sources 2022;520:230852. https://doi.org/10.1016/j.jpowsour.2021.230852.
[4] Chun O, Jamshaid F, Khan MZ, Gohar O, Hussain I, Zhang Y, Zheng K, Saleem M, Motola M, Hanif MB. Advances in low-temperature solid oxide fuel cells: an explanatory review. J Power Sources 2024;610:234719. https://doi.org/10.1016/j.jpowsour.2024.234719.

[5] Afroze S, Reza MS, Amin MR, Taweekun J, Azad AK. Progress in nanomaterials fabrication and their prospects in artificial intelligence towards solid oxide fuel cells: a review. Int J Hydrogen Energy 2024;52:216–47. https://doi.org/10.1016/j.ijhydene.2022.11.335.
[6] Vinoth Kumar R, Khandale AP. A review on recent progress and selection of cobalt-based cathode materials for low temperature-solid oxide fuel cells. Renew Sustain Energy Rev 2022;156:111985. https://doi.org/10.1016/j.rser.2021.111985.
[7] Ahmad MZ, Ahmad SH, Chen RS, Ismail AF, Hazan R, Baharuddin NA. Review on recent advancement in cathode material for lower and intermediate temperature solid oxide fuel cells application. Int J Hydrogen Energy 2022;47:1103–20. https://doi.org/10.1016/j.ijhydene.2021.10.094.
[8] Bilal Hanif M, Motola M, Gayyum S, Rauf S, Khalid A, Li CJ, Li CX. Recent advancements, doping strategies and the future perspective of perovskite-based solid oxide fuel cells for energy conversion. Chem Eng J 2022;428:132603. https://doi.org/10.1016/j.cej.2021.132603.
[9] Mehdi AM, Hussain A, Song RH, Lim TH, Kazmi WW, Ishfaq HA, Khan MZ, Qamar SU, Syed MW, Mehran MT. Improving the durability of cobaltite cathode of solid oxide fuel cells - a review. RSC Adv 2023;13:25029–53. https://doi.org/10.1039/d3ra02571c.
[10] Vostakola MF, Horri BA. Progress in material development for low-temperature solid oxide fuel cells: a review. Energies 2021;14:1280. https://doi.org/10.3390/en14051280.
[11] Baharuddin NA, Muchtar A, Somalu MR. Short review on cobalt-free cathodes for solid oxide fuel cells. Int J Hydrogen Energy 2017;42:9149–55. https://doi.org/10.1016/j.ijhydene.2016.04.097.
[12] Carda M, Budáč D, Paidar M, Bouzek K. Current trends in the description of lanthanum strontium manganite oxygen electrode reaction mechanism in a high-temperature solid oxide cell. Curr Opin Electrochem 2022;31:100852. https://doi.org/10.1016/j.coelec.2021.100852.
[13] Kaur P, Singh K. Review of perovskite-structure related cathode materials for solid oxide fuel cells. Ceram Int 2020;46:5521–35. https://doi.org/10.1016/j.ceramint.2019.11.066.
[14] Desta HG, Gebreslassie G, Zhang J, Lin B, Zheng Y, Zhang J. Enhancing performance of lower-temperature solid oxide fuel cell cathodes through surface engineering. Prog Mater Sci 2025;147:101353. https://doi.org/10.1016/j.pmatsci.2024.101353.
[15] Kane N, Zhou Y, Zhang W, Ding Y, Luo Z, Hu X, Liu M. Precision surface modification of solid oxide fuel cells via layer-by-layer surface sol-gel deposition. J Mater Chem A 2022;10:8798–806. https://doi.org/10.1039/d2ta00458e.
[16] Liu Y, Kang K, Pan Z, Wang C, Jiang K, Wang Y. Enhancing the oxygen reduction reaction activity of SOFC cathode via construct a cubic fluorite/perovskite heterostructure. Appl Surf Sci 2024;642:158405. https://doi.org/10.1016/j.apsusc.2023.158405.
[17] Shijie Z, Na L, Liping S, Qiang L, Lihua H, Hui Z. One-pot synthesis $Pr_6O_{11}$ decorated $Pr_2CuO_4$ composite cathode for solid oxide fuel cells. Int J Hydrogen Energy 2022;47:6227–36. https://doi.org/10.1016/j.ijhydene.2021.11.250.
[18] Ding X, Zhu W, Hua G, Li J, Wu Z. Enhanced oxygen reduction activity on surface-decorated perovskite $La_{0.6}Ni_{0.4}FeO_3$ cathode for solid oxide fuel cells. Electrochim Acta 2015;163:204–12. https://doi.org/10.1016/j.electacta.2015.02.084.
[19] Gu Y, Zhang Y, Zheng Y, Chen H, Ge L, Guo L. $PrBaMn_2O_{5+\delta}$ with praseodymium oxide nano-catalyst as electrode for symmetrical solid oxide fuel cells. Appl Catal, B 2019;257:117868. https://doi.org/10.1016/j.apcatb.2019.117868.
[20] Khoshkalam M, Faghihi-Sani MA, Tong X, Chen M, Hendriksen PV. Enhanced activity of $Pr_6O_{11}$ and CuO infiltrated $Ce_{0.9}Gd_{0.1}O_2$ based composite oxygen electrodes. J Electrochem Soc 2020;167:024505. https://doi.org/10.1149/1945-7111/ab6821.
[21] Caizán-Juanarena L, Zamudio-García J, Marrero-López D. Electrochemical investigation of $Pr_6O_{11}$ infiltration into $La_{0.8}Sr_{0.2}MnO_{3-\delta}$ -$Ce_{0.9}Gd_{0.1}O_{1.95}$ cathodes for IT-SOFC. Ceram Int 2023;49:33717–24. https://doi.org/10.1016/j.ceramint.2023.08.060.
[22] Sharma RK, Djurado E. An efficient hierarchical nanostructured $Pr_6O_{11}$ electrode for solid oxide fuel cells. J Mater Chem A 2018;6:10787–802. https://doi.org/10.1039/c8ta00190a.
[23] Lu X, Yang Z, Zhang J, Zhao X, Chen J, Liu W, Zhao Y, Li Y. A cobalt-free $Pr_6O_{11}$–$BaCe_{0.2}Fe_{0.8}O_{3-\delta}$ composite cathode for protonic ceramic fuel cells with promising oxygen reduction activity and hydration ability. J Power Sources 2024;599:234233. https://doi.org/10.1016/j.jpowsour.2024.234233.
[24] Taguchi H, Chiba R, Komatsu T, Orui H, Watanabe K, Hayashi K. LNF SOFC cathodes with active layer using $Pr_6O_{11}$ or Pr-doped $CeO_2$. J Power Sources 2013;241:768–75. https://doi.org/10.1016/j.jpowsour.2013.04.141.
[25] Kamecki B, Karczewski J, Jasiński P, Molin S. Improvement of oxygen electrode performance of intermediate temperature solid oxide cells by spray pyrolysis deposited active layers. Adv Mater Interfac 2021;8:2002227. https://doi.org/10.1002/admi.202002227.
[26] Ferro S. Physicochemical and electrical properties of praseodymium oxides. International Journal of Electrochemistry 2011;2011:1–7. https://doi.org/10.4061/2011/561204.
[27] Thangadurai V, Huggins RA, Weppner W. Mixed ionic-electronic conductivity in phases in the praseodymium oxide system. J Solid State Electrochem 2001;5:531–7. https://doi.org/10.1007/s100080000187.
[28] Chen T, Pang S, Shen X, Jiang X, Wang W. Evaluation of Ba-deficient PrBa1-xFe2O5+δ oxides as cathode materials for intermediate temperature solid oxide fuel cells. RSC Adv 2016;6:13829–36. https://doi.org/10.1039/c5ra19555a.
[29] Zamudio-García J, dos Santos-Gómez L, Porras-Vázquez JM, Losilla ER, Marrero-López D. Symmetrical solid oxide fuel cells based on titanate nanocomposite electrodes. J Eur Ceram Soc 2023;43:1548–58. https://doi.org/10.1016/j.jeurceramsoc.2022.11.059.
[30] Rehman SU, Hassan MH, Batool SY, Kim HS, Song RH, Lim TH, Hong JE, Joh DW, Park SJ, Lee SB. A highly stable $Co_3O_4$-GDC nanocomposite cathode for intermediate temperature solid oxide fuel cells. Int J Hydrogen Energy 2024;51:1242–54. https://doi.org/10.1016/j.ijhydene.2023.03.341.
[31] Shen Q, Huang J, Hu J, Tong Y, Chen C, Zhan Z. Impregnated LSM-YSZ electrodes with $RuO_2$/SDC nanocomposites for solid oxide cells. Int J Hydrogen Energy 2024;69:421–8. https://doi.org/10.1016/j.ijhydene.2024.04.354.
[32] Zamudio-García J, Chiabrera F, Losilla ER, Marrero-López D, Esposito V. Vertical heterostructures for symmetrical and reversible solid oxide fuel cells. Nano Energy 2024;131:110293. https://doi.org/10.1016/j.nanoen.2024.110293.
[33] Zamudio-García J, Porras-Vázquez JM, Losilla ER, Marrero-López D. Efficient symmetrical electrodes based on $LaCrO_3$ via microstructural engineering. J Eur Ceram Soc 2022;42:181–92. https://doi.org/10.1016/j.jeurceramsoc.2021.09.059.
[34] Larson AC, von Dreele RB. General structure analysis system (GSAS). Los Alamos National Laboratory; 1994.
[35] Wan TH, Saccoccio M, Chen C, Ciucci F. Influence of the discretization methods on the distribution of relaxation times deconvolution: implementing radial basis functions with DRTtools. Electrochim Acta 2015;184:483–99. https://doi.org/10.1016/j.electacta.2015.09.097.
[36] Zview, A Software program for IES analysis, Version 2.8 Scribner Associates, Inc., Southern Pines, NC (2002), (n.d.).
[37] Lin Q, Bian L, Liu C, Ting T, Liu Z, Wei P, Han S, Xu Y, Peng J, An S. Improved $La_{0.8}Sr_{0.2}MnO_{3-\delta}$ oxygen electrode activity by introducing high oxygen ion conductor oxide for solid oxide steam electrolysis. Int J Hydrogen Energy 2024;49:616–24. https://doi.org/10.1016/j.ijhydene.2023.08.316.
[38] Zamudio-García J, Caizán-Juanarena L, Porras-Vázquez JM, Losilla ER, Marrero-López D. Boosting the performance of $La_{0.8}Sr_{0.2}MnO_{3-\delta}$ electrodes by the incorporation of nanocomposite active layers. Adv Mater Interfac 2022;9:2200702. https://doi.org/10.1002/admi.202200702.
[39] Ma J, Tao Z, Kou H, Fronzi M, Bi L. Evaluating the effect of Pr-doping on the performance of strontium-doped lanthanum ferrite cathodes for protonic SOFCs. Ceram Int 2020;46:4000–5. https://doi.org/10.1016/j.ceramint.2019.10.017.
[40] Zhang Y, Zhou D, Zhu X, Wang N, Bai J, Hu L, Gong H, Zhao B, Yan W. Preparation of Pr, Co co-doped $BaFeO_{3-\delta}$-based nanofiber cathode materials by electrospinning. Int J Hydrogen Energy 2024;50:992–1003. https://doi.org/10.1016/j.ijhydene.2023.09.277.
[41] Zhang W, Zhang L, Guan K, Zhang X, Meng J, Wang H, Liu X, Meng J. Effective promotion of oxygen reduction activity by rare earth doping in simple perovskite cathodes for intermediate-temperature solid oxide fuel cells. J Power Sources 2020;446:227360. https://doi.org/10.1016/j.jpowsour.2019.227360.
[42] Raza R, Zhu B, Rafique A, Naqvi MR, Lund P. Functional ceria-based nanocomposites for advanced low-temperature (300–600 °C) solid oxide fuel cell: a comprehensive review. Mater Today Energy 2020;15:100373. https://doi.org/10.1016/j.mtener.2019.100373.
[43] Netz A, Chu WF, Thangadurai V, Huggins RA, Weppner W. Investigations of praseodymium oxide electrodes in lithium concentration cells. Ionics 1999;5:426–33. https://doi.org/10.1007/BF02376009.
[44] Burnham DA, Eyring L. Phase transformations in the praseodymium oxide-oxygen system: high-temperature X-ray diffraction studies. J Phys Chem 1968;72:4415–24. https://doi.org/10.1021/j100859a010.
[45] Vibhu V, Yildiz S, Vinke IC, Eichel R-A, Bassat J-M, de Haart LGJ. High performance LSC infiltrated LSCF oxygen electrode for high temperature steam electrolysis application. J Electrochem Soc 2019;166:F102–8. https://doi.org/10.1149/2.0741902jes.
[46] Guo Y, Chen D, Shi H, Ran R, Shao Z. Effect of Sm3+ content on the properties and electrochemical performance of $Sm_xSr_{1-X}CoO_{3-\delta}$ ($0.2 \leq x \leq 0.8$) as an oxygen reduction electrodes on doped ceria electrolytes. Electrochim Acta 2011;56:2870–6. https://doi.org/10.1016/j.electacta.2010.12.075.
[47] Jiang X, Wang J, Jia G, Qie Z, Shi Y, Idrees A, Zhang Q, Jiang L. Characterization of $PrBa_{0.92}CoCuO_{6-\delta}$ as a potential cathode material of intermediate-temperature solid oxide fuel cell. Int J Hydrogen Energy 2017;42:6281–9. https://doi.org/10.1016/j.ijhydene.2016.12.076.
[48] Dos Santos-Gómez L, Porras-Vázquez JM, Martín F, Ramos-Barrado JR, Losilla ER, Marrero-López D. An easy and innovative method based on spray-pyrolysis deposition to obtain high efficiency cathodes for Solid Oxide Fuel Cells. J Power Sources 2016;319:48–55. https://doi.org/10.1016/j.jpowsour.2016.04.034.
[49] Chen Y, Bu Y, Zhang Y, Yan R, Ding D, Zhao B, Yoo S, Dang D, Hu R, Yang C, Liu M. A highly efficient and robust nanofiber cathode for solid oxide fuel cells. Adv Energy Mater 2017;7:1601890. https://doi.org/10.1002/aenm.201601890.
[50] Xia J, Wang C, Wang X, Bi L, Zhang Y. A perspective on DRT applications for the analysis of solid oxide cell electrodes. Electrochim Acta 2020;349:136328. https://doi.org/10.1016/j.electacta.2020.136328.
[51] Osinkin DA. An approach to the analysis of the impedance spectra of solid oxide fuel cell using the DRT technique. Electrochim Acta 2021;372:137858. https://doi.org/10.1016/j.electacta.2021.137858.
[52] Abd Aziz AJ, Baharuddin NA, Somalu MR, Muchtar A. Review of composite cathodes for intermediate-temperature solid oxide fuel cell applications. Ceram Int 2020;46:23314–25. https://doi.org/10.1016/j.ceramint.2020.06.176.
[53] Fan X, You CY, Zhu JL, Chen L, Xia CR. Fabrication of LSM-SDC composite cathodes for intermediate-temperature solid oxide fuel cells. Ionics 2015;21:2253–8. https://doi.org/10.1007/s11581-015-1396-0.
[54] Nam S, Kim J, Kim H, Ahn S, Jeon SH, Choi Y, Park BK, Jung WC. Revitalizing oxygen reduction reactivity of composite oxide electrodes via electrochemically

deposited $PrO_x$ nanocatalysts. Adv Mater 2024;36:2307286. https://doi.org/10.1002/adma.202307286.
[55] Jeon Y, ha Myung J, hoon Hyun S, gun Shul Y, Irvine JTS. Corn-cob like nanofibres as cathode catalysts for an effective microstructure design in solid oxide fuel cells. J Mater Chem A 2017;5:3966–73. https://doi.org/10.1039/c6ta08692f.
[56] Zamudio-García J, Caizán-Juanarena L, Porras-Vázquez JM, Losilla ER, Marrero-López D. Unraveling the influence of the electrolyte on the polarization resistance of nanostructured $La_{0.6}Sr_{0.4}Co_{0.2}Fe_{0.8}O_{3-\delta}$ cathodes. Nanomaterials 2022;12:3936. https://doi.org/10.3390/nano12223936.
[57] Chen XJ, Khor KA, Chan SH. Identification of $O_2$ reduction processes at yttria stabilized zirconia|doped lanthanum manganite interface. J Power Sources 2003;123:17–25. https://doi.org/10.1016/S0378-7753(03)00436-1.
[58] Siebert E, Hammouche A, Kleitz M. Impedance spectroscopy analysis of $La_{1-x}Sr_{itx}MnO_3$-yttria-stabilized zirconia electrode kinetics. Electrochim Acta 1995;40:1741–53. https://doi.org/10.1016/0013-4686(94)00361-4.
[59] Kuai X, Yang G, Chen Y, Sun H, Dai J, Song Y, Ran R, Wang W, Zhou W, Shao Z. Boosting the activity of $BaCo_{0.4}Fe_{0.4}Zr_{0.1}Y_{0.1}O_{3-\delta}$ perovskite for oxygen reduction reactions at low-to-intermediate temperatures through tuning B-site cation deficiency. Adv Energy Mater 2019;9:1902384. https://doi.org/10.1002/aenm.201902384.
[60] Liu Z, Zhao Z, Shang L, Ou D, Cui D, Tu B, Cheng M. LSM-YSZ nano-composite cathode with YSZ interlayer for solid oxide fuel cells. J Energy Chem 2017;26:510–4. https://doi.org/10.1016/j.jechem.2016.11.019.
[61] Jiang Z, Zhang L, Cai L, Xia C. Bismuth oxide-coated (La,Sr)$MnO_3$ cathodes for intermediate temperature solid oxide fuel cells with yttria-stabilized zirconia electrolytes. Electrochim Acta 2009;54:3059–65. https://doi.org/10.1016/j.electacta.2008.11.067.
[62] Zhang X, Wu W, Zhao Z, Tu B, Ou D, Cui D, Cheng M. Insight into the oxygen reduction reaction on the LSM|GDC interface of solid oxide fuel cells through impedance spectroscopy analysis. Catal Sci Technol 2016;6:4945–52. https://doi.org/10.1039/c5cy02232k.
[63] Tsai T, Barnett SA. Effect of LSM-YSZ cathode on thin-electrolyte solid oxide fuel cell performance. Solid State Ionics 1997;93:207–17. https://doi.org/10.1016/S0167-2738(96)00524-3.
[64] Kao WX, Lee MC, Chang YC, Lin TN, Wang CH, Chang JC. Fabrication and evaluation of the electrochemical performance of the anode-supported solid oxide fuel cell with the composite cathode of $La_{0.8}Sr_{0.2}MnO_{3-\delta}$-Gadolinia-doped ceria oxide/$La_{0.8}Sr_{0.2}MnO_{3-\delta}$. J Power Sources 2010;195:6468–72. https://doi.org/10.1016/j.jpowsour.2010.04.057.
[65] Chen K, Lü Z, Ai N, Chen X, Hu J, Huang X, Su W. Effect of SDC-impregnated LSM cathodes on the performance of anode-supported YSZ films for SOFCs. J Power Sources 2007;167:84–9. https://doi.org/10.1016/j.jpowsour.2007.01.088.
[66] Li J, Wang S, Wang Z, Liu R, Wen T, Wen Z. $La_{0.84}Sr_{0.16}MnO_{3-\delta}$ cathodes impregnated with $Bi_{1.4}Er_{0.6}O_3$ for intermediate-temperature solid oxide fuel cells. J Power Sources 2009;194:625–30. https://doi.org/10.1016/j.jpowsour.2009.06.070.
[67] Jiang Z, Lei Z, Ding B, Xia C, Zhao F, Chen F. Electrochemical characteristics of solid oxide fuel cell cathodes prepared by infiltrating (La,Sr)$MnO_3$ nanoparticles into yttria-stabilized bismuth oxide backbones. Int J Hydrogen Energy 2010;15:8322–30. https://doi.org/10.1016/j.ijhydene.2009.12.008.